Journal of Nuclear Materials 442 (2013) 282–291

Contents lists available at ScienceDirect

Journal of Nuclear Materials

journal homepage: www.elsevier.com/locate/jnucmat

On the thermal stability of late blooming phases in reactor pressure vessel steels: An atomistic study

G. Bonny [a,*], D. Terentyev [a], A. Bakaev [a,b,c], E.E. Zhurkin [c], M. Hou [d], D. Van Neck [b], L. Malerba [a]

[a] SCK•CEN, Nuclear Materials Science Institute, Boeretang 200, B-2400 Mol, Belgium
[b] Ghent University, Center for Molecular Modeling, Technologiepark 903, B-9052 Zwijnaarde, Belgium
[c] Saint-Petersburg State Polytechnical University, Experimental Nuclear Physics Department, K-89, Faculty of Physics and Mechanics, 29 Polytekhnicheskaya Str., 195252 St. Petersburg, Russia
[d] Université Libre de Bruxelles, CP223, Faculté des Sciences, Bd du Triomphe, B-1050 Bruxelles, Belgium

ARTICLE INFO

Article history:
Received 1 June 2013
Accepted 12 August 2013
Available online 3 September 2013

ABSTRACT

Radiation-induced embrittlement of bainitic steels is the lifetime limiting factor of reactor pressure vessels in existing nuclear light water reactors. The primary mechanism of embrittlement is the obstruction of dislocation motion produced by nanometric defect structures that develop in the bulk of the material due to irradiation. In view of improving the predictive capability of existing models it is necessary to understand better the mechanisms leading to the formation of these defects, amongst which the so-called "late blooming phases". In this work we study the stability of the latter by means of density functional theory (DFT) calculations and Monte Carlo simulations based on a here developed quaternary FeCuNiMn interatomic potential. The potential is based on extensive DFT and experimental data. The reference DFT data on solute–solute interaction reveal that, while Mn–Ni pairs and triplets are unstable, larger clusters are kept together by attractive binding energy. The NiMnCu synergy is found to increase the temperature range of stability of solute atom precipitates in Fe significantly as compared to binary FeNi and FeMn alloys. This allows for thermodynamically stable phases close to reactor temperature, the range of stability being, however, very sensitive to composition.

1. Introduction

Radiation-induced embrittlement of bainitic steels is the lifetime limiting factor of the irreplaceable reactor pressure vessels (RPV) in existing nuclear light water reactors (LWR). The primary mechanism of embrittlement is the obstruction of dislocation motion produced by nanometric defect structures that develop in the bulk of the material due to irradiation. Two classes of nano-structural features are considered as the main contributors to the embrittlement of RPV steels, both hardly visible in the electron microscope: (a) clusters of solute atoms such as Cu, Ni, and Mn, generally catalogued as precipitates; and (b) the so-called 'matrix damage', generally interpreted in terms of clusters of point-defects [1–3].

In the first class of features, one can further distinguish between Cu-rich precipitates (CRPs) [2] and Mn–Ni-rich precipitates (MNPs) [4]. The formation of the latter, which might also not contain Cu, is favoured by low(er) temperature and high Ni (and Mn and Si) content [3]. MNPs without Cu are detected only at sufficiently high neutron fluence, not only in (low-Cu) RPV steels [5,6], but also in FeMnNi model alloys [6,7]. Moreover, based on simplified thermodynamic-kinetic models briefly recalled below, there is a belief that precipitates rich in Mn and Ni, once nucleated, will rapidly grow to large volume fractions [3]. For these reasons, they are more commonly denoted as *late blooming phases* (LBP), or confused with them. Their appearance has been associated with the possibility of a sudden and unexpected increase of embrittlement above a certain dose, that cannot be predicted by current commonly used empirical correlations [2,3], thereby posing a question mark on the possibility of extending the lifetime of existing LWR.

In view of improving the predictive capability of existing models it is necessary to understand better the mechanisms leading to the formation of these so-called LBPs, to investigate their stability and to assess their strength as obstacles to dislocation motion. The possibility of forming Cu free MNPs was put forward for the first time in [8], based on regular solution theory calculations and equilibrium lattice Monte Carlo simulations, parameterized purely on the basis of thermodynamic considerations [2–4,9]. These early simulations led to the conclusion that it is thermodynamically favourable for Mn, Ni and Si to precipitate and form clusters at the interface around a core of Cu. Moreover, the results of the simulations suggested that lower temperature and lower Cu content, or higher Mn, Ni and Si content, would favour Mn, Ni and Si

* Corresponding author.
E-mail address: gbonny@sckcen.be (G. Bonny).

0022-3115/$ - see front matter © 2013 Elsevier B.V. All rights reserved.
http://dx.doi.org/10.1016/j.jnucmat.2013.08.018

enrichment of these clusters. The model did not include, however, any description of the mechanisms of precipitation by diffusion, nor any detail about solute/point-defect interaction. It was indeed explicitly assumed that MNPs, as well as CRPs, are stable thermodynamic phases, the formation of which is enhanced under irradiation, and would be more frequently found in low-Cu steels, especially if temperature is low (265 °C versus the usual 288 °C) and dose is fairly high [2,4,8,9].

In a recent study [10], a more advanced simulation methodology was used to investigate the physical mechanism of formation of LBPs. Namely, an atomistic kinetic Monte Carlo model parameterized on electronic structure calculations data was used to study the formation and evolution under irradiation of solute clusters in FeMnNi ternary and FeCuMnNi quaternary alloys. Two populations of clusters were observed to form, which can be discriminated by whether or not the solute atoms are associated with self-interstitials and their clusters. MnNi-rich clusters, that invariably contained a large majority of self-interstitials, were observed to form at a very early stage of the irradiation in both modelled alloys; the quaternary alloys contained also self-interstitial-free, Cu-containing clusters. MnNi-rich clusters nucleated very early via a self-interstitial-driven mechanism, earlier than Cu-rich clusters; the latter, however, grew in number much faster than the former, helped by the strong thermodynamic driving force to Cu precipitation in Fe, thereby becoming dominant in the low dose regime. The kinetics of the number density increase of the two populations was thus significantly different. The somewhat provocative conclusion of that work was that the so-called *late blooming phase*s might well be neither *late*, nor *phases*. Indeed, a specific feature of the model used in [10] was that the precipitation of Ni and Mn due to thermodynamic driving forces was implicitly excluded, as a consequence of the fact that the density functional theory (DFT) calculations used to parameterize the model predicted repulsion between Ni and Mn pairs in Fe. Even so, Ni and Mn clusters did form, at very low doses, catalysed by the presence of self-interstitials, thereby showing that the thermodynamic stability of these clusters as phases is *not a necessary condition* for their appearance under irradiation. The intimate relationship between solutes and self-interstitials also casts some doubts on the physical justification of distinguishing between "precipitates" and "matrix damage" as two separate classes of embrittling features.

Nonetheless, the work in [10] left open the question of whether or not NiMn(Si) clusters may or not be regarded as thermodynamic phases and, if so, under which conditions and with which range of stability. As a matter of fact, considering the FeMn and FeNi binary alloys separately, the respective phase diagrams indicate that the solubility limits of Mn and Ni in α-Fe at 300 °C are approximately 3 and 4 wt% respectively [11–14], i.e., significantly higher than the typical Ni and Mn content in RPV steels. Nonetheless, the solubility limit provided for the *ternary* FeMnNi alloy (TCFE5 database) by the *Thermocalc* software [15] (0.64 at.% and 0.2 at.% at 300 °C for Mn and Ni, respectively [7]) is significantly lower, denoting a strong synergy between Ni and Mn in Fe. *Thermocalc* uses an experimental database of thermodynamic functions, extrapolated whenever the available data are insufficient, to calculate the phase diagram of most alloys, based on free energy functions of temperature and concentration and common tangent construction (Computer Coupling of Phase Diagrams and Thermochemistry: Calphad database and formalism). Quite clearly, extrapolation to temperatures for which it is difficult to obtain experimental calorimetric data is always uncertain. In particular, the data for the MnNi interaction used in Calphad originate from an extrapolation of experiments realized by Dinsdale at temperatures ~400 °C [16]. The difference between the results of the DFT-informed model in [10] and the *Thermocalc* results arises from the nature of the MnNi interaction, which is attractive in the Calphad database, while it is repulsive according to so far available DFT calculations [17]. Thus, there seems to be a discrepancy between DFT and Calphad and a good part of the present work is devoted to investigating whether this discrepancy is real or not and whether it can be removed and, if so, how.

This is done by performing new DFT calculations to be used, together with experimental phase diagram indications, to develop a thermodynamically consistent interatomic potential for the FeCuNiMn system. We show that, even though DFT calculations predict instability of Ni–Mn pairs and triplets, Ni–Mn clusters become stable above a certain size. By informing the interatomic potential to this new insight, as well as to other experimental reference data, it becomes possible to use it as a reliable tool to study phase stability in the FeCuNiMn system. The use of appropriate Metropolis Monte Carlo techniques to build the phase diagram of the quaternary alloy from the potential allows us in this work, therefore, to give a reasonable *ab initio*, rather than experimental, estimate of the range of temperature and concentration in which MnNi(Cu) precipitates in Fe can be considered as thermodynamically stable phases, as well as the expected equilibrium concentration of Ni and Mn in those phases.

The advantage of fitting an interatomic potential over building a purely thermodynamic model is that the former can also be fitted, up to a certain extent, to reproduce the interaction of solute atoms with point-defects and their clusters. This is done and partly tested in the present work, opening the way to the study of complexes composed of both point-defects and solute atoms. The ultimate objective is that the interaction of these nanofeatures with dislocations can be investigated quantitatively. As a matter of fact, irrespective of whether solute clusters in RPV steels are or are not thermodynamically stable phases, their association (or not) with point-defect clusters, especially self-interstitial clusters, will influence not only their kinetics of formation and stability, but also, and more importantly, the strength that they oppose as obstacles to dislocation motion.

2. Methods and formalisms

2.1. Density functional theory calculations

The DFT calculations were performed using the Vienna *ab initio* simulation package (VASP) [18,19]. VASP is a plane-wave DFT code that implements the Projector Augmented Wave (PAW) method [20,21]. Standard PAW potentials supplied with VASP were used, with exchange and correlation functional described by the Perdew–Wang parameterization [22] in the Generalised Gradient Approximation (GGA), with a Vosko–Wilk–Nusair interpolation [23]. For Fe, Cu, Ni and Mn pseudo potentials with 8, 11, 10 and 7 valence electrons were used, respectively.

Finite temperature smearing was obtained following the Methfessel–Paxton method with a smearing width of 0.3 eV. The plane-wave cut-off energy was set to 300 eV, which proved sufficient for convergence of the binding and migration energy of the selected configurations. Brillouin zone sampling was performed using the Monkhorst–Pack scheme, where meshes of $3 \times 3 \times 3$ k-points proved sufficient for convergence. The total energy was calculated in periodic bcc supercells containing 128 atoms in a fixed volume set to the equilibrium volume of Fe.

For the defect-solute and solute–solute interactions the total binding energy of a configuration containing n objects ($i = 1...n$) X_i is defined as,

$$E_b(X_1 \ldots X_n) = \sum_i E(X_i) - \left[E\left(\sum_i X_i \right) + (n-1) E_{ref} \right], \quad (1)$$

where E_{ref} is the energy of the supercell without any objects (pure bcc Fe), $E(X_i)$ is the energy of the supercell containing the single

object X_i, and $E(\sum_i X_i)$ is the energy of the supercell containing all interacting objects. Within this definition positive values of E_b denote attraction.

We note that for spin-polarized calculations concerning antiferromagnetic solutes we took special care in selecting the initial value of the magnetic moments, so as to ensure that the true minimum energy configuration was obtained. In the paper we report the results corresponding to the lowest energy configurations only.

2.2. Interatomic potential

The atomic interactions are described here using the embedded atom method (EAM) [24], which is widely used to describe metals and their alloys. In addition to pair interactions, V, this approach includes an embedding energy, F, that depends on the local electron density, ρ. The latter term approximates the many-body contribution of all nearby atoms. The total energy within the EAM is given as,

$$E = \frac{1}{2}\sum_{\substack{i,j=1\\ j\neq i}}^{N} V_{t_i t_j}(r_{ij}) + \sum_{i=1}^{N} F_{t_i}(\rho_i), \tag{2}$$

Here N represents the total number of atoms in the system, r_{ij} is the distance between atoms i and j, and t_i denotes chemical species (Fe, Ni, Cu or Mn in our case). The local electron density around atom i, contributed from its neighbours, is given as,

$$\rho_i = \sum_{\substack{j=1\\ j\neq i}}^{N} \varphi_{t_j}(r_{ij}), \tag{3}$$

where φ denotes the electron density function of the considered element. Thus, for the FeNiCuMn quaternary system 18 functions need to be defined: φ_{Fe}, φ_{Ni}, φ_{Cu}, φ_{Mn}, F_{Fe}, F_{Ni}, F_{Cu}, F_{Mn}, V_{FeFe}, V_{NiNi}, V_{CuCu}, V_{MnMn}, V_{FeNi}, V_{FeCu}, V_{FeMn}, V_{NiCu}, V_{NiMn}, and V_{CuMn}.

In this work we use as starting point the state-of-the-art ternary FeNiCu potential [25]. In this potential, the Fe part is taken from Mendelev et al. [26] ('potential 2'), the Cu part from Mishin et al. [27] ('EAM 1') and the Ni part from Voter and Chen [28]. The Fe potential has been widely used, tested and has demonstrated so far to be the one that succeeds at best in reproducing the properties of iron that are of interest for radiation damage studies [29], including dislocation properties [30]. The Cu and Ni potentials, though not specifically developed to model radiation damage, represent state-of-the-art potentials that are suitable for our purposes. The Fe–Cu, Fe–Ni and Ni–Cu interactions in this potential were fitted using the experimental phase diagram as direct reference, while following DFT indications to fit the point-defect/solute-atom interaction and vacancy migration barriers, as described in [25,31,32].

In the literature we found two modified embedded atom method (MEAM) potentials to describe Mn, developed by Torelli et al. [33] and Kim et al. [34]. However, for reasons of compatibility with the ternary EAM type FeNiCu potential a Mn potential of EAM type is desirable. Thus, six functions remain to be fitted in the present work: φ_{Mn}, F_{Mn}, V_{MnMn}, V_{FeMn}, V_{NiMn}, and V_{CuMn}. Similarly to the FeNiCu potential, we target for the fitting the experimental phase diagram, as well as both experimental and DFT indications concerning point-defect/solute-atom interaction and vacancy migration barriers. The methodology used to do so is detailed in [35] and the parameterization of the fitted functions is given in Appendix A. In Sections 3 and 4 the data selected for the fitting are discussed.

As DFT indication we used three different data sets: our own calculations (detailed in Section 2.1), another PAW-based data set and a data set obtained using ultra soft pseudo potentials (USPP). The references to the latter two data sets are given in the caption text of the tables with initial ab initio fitting data. As a general rule, priority was given to the USPP data set for reasons of consistency, as the FeNiCu potential was also fitted to that data set. In the absence of USPP data or in the necessity of a trade-off, other data were used.

2.3. Monte Carlo calculations

In this work the phase boundaries were estimated by means of Metropolis Monte Carlo (MC) sampling [36] within the isobaric semi-grand canonical ensemble (N, P, T, $\Delta\mu$) for binaries and isobaric grand canonical ensemble (N, P, T) for ternary and quaternary, respectively. Both MC methods include three types of trials of which two are common to both methods: (i) a random displacement of all atoms from their current positions (by this trial lattice relaxation and vibrational entropy are accounted for); (ii) the overall volume change of the simulation box (this trial allows the desired pressure to be maintained, even if a structural transition was to occur). In the semi-grand canonical ensemble the third trial consists of the change of species of a randomly picked atom (by this trial the equilibrium composition is sampled), while in the grand canonical ensemble the latter consists of the random exchange of two atoms of different species (by this trial the equilibrium configurations are sampled). The decision on the acceptance of the new configuration is based on the standard Metropolis algorithm [36] and one set of these trials is termed an "MC step".

The phase boundaries are obtained by scanning the chemical potential difference, $\Delta\mu$ versus composition. A plot of such a curve is obtained at every desired temperature and any discontinuity in the latter is interpreted as a phase transition (see [37] and references therein for more details). In order to identify the solubility limit at a given temperature, the average composition of the last three points (which show statistical scatter) is taken before the phase transition occurs, the maximum spread in the latter serving as error bar.

The ternary and quaternary phase boundaries are obtained by scanning the temperature (50 K temperature grid) for different compositions (0.5–2% Ni or Mn and 0–0.5% Cu). In this way the phase boundary was established by visual inspection of precipitation. The disadvantage of such simulations compared to the ones for the binaries is that they are lengthy (typically 5×10^6 MC steps after thermalization by molecular dynamics) and large box sizes are necessary (containing 21,296 atoms) to minimize surface effects. On the other hand, the advantage is that these simulations are simple and provide precise information on the precipitate morphology and composition.

3. Manganese: DFT data and interatomic potential

Pure manganese undergoes the following allotropic transformations: (i) the ground state is non-collinear anti-ferromagnetic α-Mn (Strukturbericht A12) with Néel temperature T_N = 98 K, (ii) at 1000 K paramagnetic β-Mn is stabilized (Strukturbericht A13), (iii) in the range 1368–1406 K γ-Mn appears (fcc – Strukturbericht A1), (iv) from 1406 K up to melting point, T_M = 1517 K, δ-Mn is the stable structure (bcc – Strukturbericht A2). The three independent elastic constants obtained from experiment (on polycrystals) for α-Mn are C_{11} = 203 GPa, C_{12} = 33 GPa and C_{44} = 85 GPa (values are for the anti-ferromagnetic phase at 4 K and are similar to the ones observed in the paramagnetic phase [38]). This yields a bulk modulus, $B = \frac{1}{3}(C_{11} + 2C_{12})$, of 90 GPa, which is compatible within the range of values found in other experiments, namely: 60 GPa [39], 93 GPa [40], 131 GPa [41], 137 GPa [42] and 158 GPa [43].

The experimental elastic constants reveal a negative Cauchy pressure, $\frac{1}{2}(C_{12}-C_{44})$, of −26 GPa. As reported in [44], this fact points towards angularity in the bonding which cannot be captured within a many-body central framework such as the EAM formalism [45–47]. Since the development of an angular dependent Mn potential is outside the scope of this work (the potential is not meant to describe pure Mn, but Mn as alloying element in Fe: the Mn content in Western-type LWR pressure vessel steels is at most a few per cents) and is incompatible with our EAM type FeNiCu potential, we tried to stabilize α-Mn with modified elastic constants to give a slightly positive Cauchy pressure but conservation of bulk modulus. All such trials, however, met with failure. Either α-Mn was not the ground state structure, or the embedding function had a negative curvature, which is physically unacceptable. It is interesting to note, from an EAM fitting viewpoint, that the stabilization of α-Mn seemed to be closely correlated to a negative Cauchy pressure.

Given the failure to produce an EAM type potential that stabilizes α-Mn as the ground state, we alternatively chose γ-Mn as the ground state. This choice can be justified as in metallurgy Mn is known to be an austenizer when added as solute in iron [48]. To obtain the target cohesive energy for γ-Mn and the competing δ-Mn and ε-Mn (hcp – Strukturbericht A3) we used DFT calculated energy differences reported in [49,50] (see Table 1) with as reference the experimentally measured cohesive energy for α-Mn, E_c = 2.92 eV [51]. However, from these values ε-Mn is stabilized over γ-Mn, which in reality is only expected to stabilize under high pressure [43]. To avoid this complexity, we opted to fit a short range EAM potential such that both hcp and fcc structures are degenerate. We also mention here that the γ-δ energy difference predicted by DFT was chosen as reference instead of the Calphad data, because the latter gave rise to a potential with fcc/bcc transition temperature below 300 K.

No experimental value is available for the elastic constants of γ-Mn. Therefore we performed DFT calculations on antiferromagnetic (AFM) crystals ($L1_0$ ordered ground state [50]) and non-magnetic (NM) crystals (emulating the paramagnetic state – experimentally an anti-ferromagnetic – paramagnetic transition is observed in quenched γ-Mn crystals at ∼500 K [53,54]). The DFT results obtained for the three independent elastic constants are summarized in Table 1. We observe a large discrepancy between AFM and NM calculations, especially for the bulk modulus. This is consistent with similar calculations performed on α-Mn [49] and β-Mn [50]. Given the softness of Mn and the small discrepancy between the elastic constants measured in anti-ferromagnetic and paramagnetic α-Mn crystals, we believe that our anti-ferromagnetic results seem the most reasonable input. It must be noted, however, that the AFM results yield a negative Cauchy pressure of −52 GPa. For the sake of fitting an EAM-type Mn potential, however, we have (artificially) chosen a small but positive Cauchy pressure of 10 GPa as target value. The bulk modulus B and C', on the other hand, were kept as obtained from the DFT calculations (see Table 1). The latter modifications should have little or no influence when studying Fe-rich alloys.

The fcc/bcc transition and melting temperature of the potential were obtained by means of thermodynamic integrations [55,56]. By performing the latter we obtained the Helmholtz free energy of the fcc and bcc phase as well as the Gibbs free energy of the liquid phase as a function of temperature. We note that for the solid phases we constrained the volume to avoid allotropic transformations during the thermodynamic integration. As a result, the transition from fcc to bcc and bcc to liquid were estimated from the intersections of the respective free energy curves. The results of this procedure are summarized in Table 1.

Having discussed all desired properties of the Mn potential, its actual properties are summarized and compared to DFT, Calphad and experimental data in Table 1. Given the above discussed constraints and the expected use of the potential, we consider its performance adequate for our purposes.

Table 1
Comparison of basic properties of Mn with predictions by the potential.

Property	Experiment or calculation	Potential
E_c(γ-Mn) (eV/atom)	2.888[a]/2.853[b]	2.889
ΔE_c(γ–δ) (eV/atom)	0.008[c]/0.079[d]	0.081
ΔE_c(γ–ε) (eV/atom)	−0.010[c]/−0.006[d]	0.000
a_0(γ-Mn) (Å)	3.750[e]/3.547[d]/3.551[f]/3.496[g]	3.496
a_0(δ-Mn) (Å)	2.812[d]	2.812
a_0(ε-Mn) (Å)	–	Ideal a/c ratio
B(GPa)	99[f]/251[g]	99
C'(GPa)	35[f]/84[g]	35
½(C_{12}–C_{44}) (GPa)	−52[f]/3[g]	10
$T_{fcc\rightarrow bcc}$ (K)	1406	1127 ± 40
$T_{bcc\rightarrow liq}$ (K)	1517/1411[c]	1353 ± 40

[a] Based on experiment and Calphad assessment, Refs. [12,51].
[b] Based on experiment and DFT calculations, Refs. [49–51].
[c] Calphad assessment, Ref. [12].
[d] DFT calculations, Refs. [49,50].
[e] Experiment, Ref. [52].
[f] DFT, this work, calculations in anti-ferromagnetic ground state ($L1_0$ magnetic ordering).
[g] DFT, this work, calculations in non-magnetic ground state.

4. The quaternary alloy: DFT data and interatomic potentials

4.1. Iron-manganese

In Table 2 point-defect properties of Mn in a bcc Fe matrix calculated by both DFT and the potential are summarized. Properties that were explicitly targeted during the fit of the potential are indicated with the symbol ∗.

In general, the USPP data set predicts less binding or more repulsion than the PAW data set. Although they generally predict the same trend, there are some striking qualitative differences: repulsion (USPP) versus attraction (PAW) of Mn–Mn pairs and repulsion versus neutral interaction for Mn in the tensile region of a ⟨1 1 0⟩ self-interstitial atom (SIA). Given the quantitative uncertainty and qualitative indefiniteness in the binding energy for

Table 2
Comparison of point-defect Mn-solute properties in the bcc Fe matrix between DFT and the potential.

Property	DFT (eV)	Potential (eV)
E_b Mn–Mn (1nn)*	−0.28[a]/0.08[b]	0.02
E_b Mn–Mn (2nn)*	−0.20[a]/0.04[b]	0.01
E_b Mn–Vac (1nn)	0.12[a]/0.21[b]	−0.02
E_b Mn–Vac (2nn)	0.07[a]/0.14[b]	0.00
E_f⟨1 1 0⟩ (Mn)	3.70[c]	4.69
E_f⟨1 1 1⟩–E_f ⟨1 1 0⟩ (Mn)	0.63[c]	0.37
E_f⟨1 0 0⟩–E_f ⟨1 1 0⟩ (Mn)	1.15[c]	0.72
E_f(Octa)–E_f ⟨1 1 0⟩ (Mn)	1.26[c]	0.77
E_f(Tetra)–E_f ⟨1 1 0⟩ (Mn)	0.42[c]	0.79
E_b⟨1 1 0⟩ Fe–Mn*	0.37[d]/0.57[b]	0.37
E_b SIA Mn in tension	−0.36[d]/0.03[b]	0.01
E_b SIA Mn in compression	0.10[d]/0.35[b]	0.07
E_b⟨1 1 0⟩ Fe–Mn, Mn in compression	0.29[d]	0.31
E_b⟨1 1 0⟩ Mn–Mn	0.47[d]	0.33
E_b Fe–Mn crowdion	0.66[b]	0.49
E_m(Vac → Mn)*	1.03[a]/0.93[b]	1.06
E_m(⟨1 1 0⟩ → ⟨0 1 1⟩) (Mn)	0.34[d]	0.34

[a] DFT, USPP, Ref. [58].
[b] DFT, PAW, Ref. [59].
[c] DFT, PAW, this work.
[d] DFT, USPP, Ref. [60].

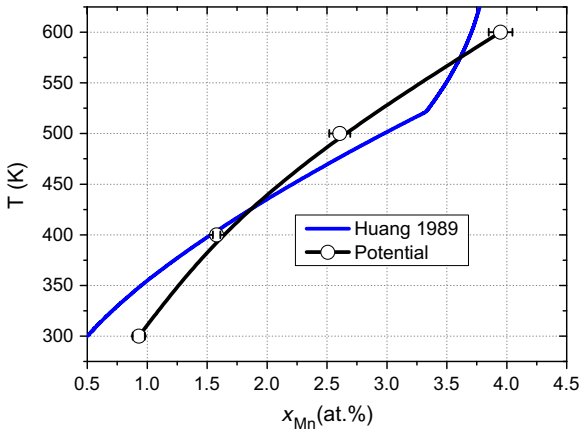

Fig. 1. Comparison between experimental Mn solubility and the one obtained from the potential.

Mn–Mn pairs, we decided to keep its value small and make a close fit to the FeMn experimental solubility limit (see Fig. 1). We note that, given this constraint, it proved impossible to fit a significant Mn-vacancy binding. Any effort to try to do so resulted in a strong underestimation of Mn solubility, and given the study at hand we opted for reproducing the latter correctly.

From the DFT calculated formation energy of the different interstitial Mn configurations, summarized in Table 2, it is clear that the ⟨1 1 0⟩ mixed dumbbell is the most favourable configuration. In addition, the latter configuration gives a strong binding energy, as well as the Mn crowdion. All these important effects are well reproduced by the potential. From the other interstitial configurations summarized in Table 2 we learn that Mn essentially behaves as an undersized atom as it exhibits binding in compressed zones and even allows for a stable ⟨1 1 0⟩ MnMn mixed dumbbell. Again, all these effects are well reproduced by the potential.

Finally, we mention that the Mn-vacancy exchange barrier and Mn Johnson jump [57] are in excellent agreement with the DFT values.

The Fe-rich phase boundary obtained with the potential is compared with the Calphad calculated one [12] in Fig. 1. The kink in the Calphad curve observed around ∼520 K is of magnetic origin and cannot be reproduced within an EAM framework. Nevertheless, the agreement between potential and Calphad calculations is satisfactory.

4.2. Iron–manganese–nickel

In Table 3 properties of small NiMn clusters in a bcc Fe matrix calculated by both DFT and the potential are summarized. Properties that were explicitly targeted during the fitting of the potential are indicated with the symbol ∗.

Considering the DFT data first, we observe that pure Mn and Ni clusters in Fe are binding, Mn clusters being the most stable ones. Mixed NiMn clusters, on the other hand, are repulsive for clusters up to size 3 and stable starting from size 4. Thus the apparent contradiction between DFT and Calphad, discussed in the introduction, is resolved if large enough clusters (>size 4) are taken.

However, when fitting a potential with repulsive NiMn pairs, it is impossible to stabilize mixed clusters, irrespective of the size. Therefore we opted for fitting a small but binding value also for NiMn pairs, even though this is at variance with DFT, and use the experimental NiMn phase diagram as additional fitting input. Given this constraint and as shown in Table 3, we observe that the potential does allow for the formation of mixed NiMn clusters.

Table 3
Comparison of the binding energy of MnNi clusters in the bcc Fe matrix between DFT and the potential.

Property	DFT (eV)	Potential (eV)
E_b Ni–Mn (1nn)*	−0.06[a]/0.00[b]	0.01
E_b Ni–Mn (2nn)*	−0.06[a]/−0.08[b]	0.00
E_b triangle Mn_3	0.11[b]	0.05
E_b triangle $NiMn_2$	−0.05[b]	0.03
E_b triangle Ni_2Mn	−0.01[b]	0.13
E_b triangle Ni_3	0.05[b]	0.06
E_b tetrahedron Mn_4	0.20[b]	0.10
E_b tetrahedron $NiMn_3$	0.08[b]	0.08
E_b tetrahedron Ni_2Mn_2 (Ni 1nn)	0.00[b]	0.02
E_b tetrahedron Ni_2Mn_2 (Ni 2nn)	0.02[b]	0.16
E_b tetrahedron Ni_3Mn	0.05[b]	0.08
E_b tetrahedron Ni_4	0.10[b]	0.09
E_b⟨1 1 0⟩ Ni–Mn*	0.12[c]	0.12

[a] DFT, USPP, Ref. [58].
[b] DFT, PAW, this work.
[c] DFT, USPP, Ref. [60].

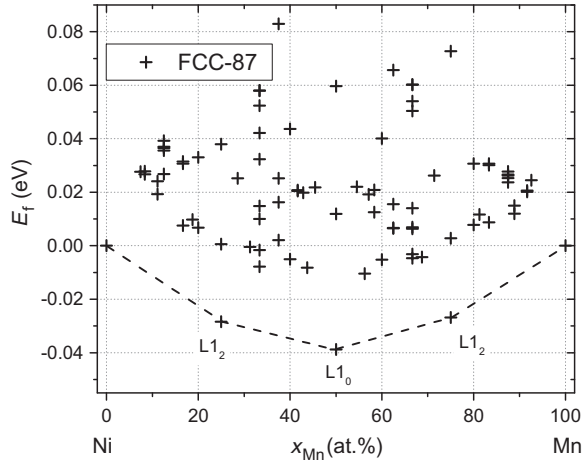

Fig. 2. Possible ground state intermetallics of the NiMn system at zero Kelvin as obtained by the potential.

Finally, we mention that the ⟨1 1 0⟩ NiMn dumbbell is stable with the potential and reproduces the DFT value.

In Fig. 2 the zero Kelvin phase diagram is presented in the form of a superposition of possible ground state intermetallics, i.e., FCC-87 ground state structures (see [35] for more details). Briefly, for the desired intermetallics to be true ground states of the system, all other candidate states should lie above the convex hull of the latter. As shown in Fig. 2, the potential only stabilizes experimentally observed intermetallic phases, which are: the $L1_2$ Ni_3Mn, $NiMn_3$ and $L1_0$ NiMn phases [61–63].

4.3. Iron–manganese–copper

In Table 4 properties of small CuMn clusters in a bcc Fe matrix calculated by both DFT and the potential are summarized. Properties that were explicitly targeted during the fitting of the potential are indicated with the symbol ∗.

The DFT data on the CuMn pairs predict weak attraction at 1nn and weak repulsion at 2nn distance. Given the uncertainty in the DFT data we gave priority to a close reproduction of the Mn solubility limit in Cu. With respect to clusters, both DFT and the potential predict binding for all configurations, with the binding energy monotonically increasing as Mn atoms are replaced by Cu ones. This trend is supported by experiments, where a small Cu

Table 4
Comparison of the binding energy of MnCu clusters in the bcc Fe matrix between DFT and the potential.

Property	DFT (eV)	Potential (eV)
E_b Cu–Mn (1nn)*	0.04[a]/0.13[b]	0.04
E_b Cu–Mn (2nn)*	−0.07[a]/−0.02[b]	0.02
E_b triangle Mn_3	0.11[b]	0.05
E_b triangle $CuMn_2$	0.18[b]	0.08
E_b triangle Cu_2Mn	0.34[b]	0.16
E_b triangle Cu_3	0.51[b]	0.24
E_b tetrahedron Mn_4	0.20[b]	0.10
E_b tetrahedron $CuMn_3$	0.32[b]	0.15
E_b tetrahedron Cu_2Mn_2 (Cu 1nn)	0.35[b]	0.22
E_b tetrahedron Cu_2Mn_2 (Cu 2nn)	0.41[b]	0.26
E_b tetrahedron Cu_3Mn	0.66[b]	0.35
E_b tetrahedron Cu_4	0.92[b]	0.48
$E_b\langle 110\rangle$ Cu–Mn*	−0.06[c]	−0.06

[a] DFT, USPP, Ref. [58].
[b] DFT, PAW, this work.
[c] DFT, USPP, Ref. [60].

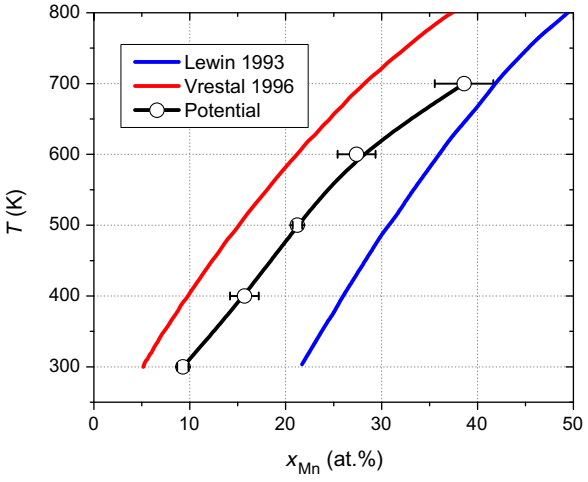

Fig. 3. Comparison between CuMn phase diagrams resulting from thermodynamic models and the potential.

solubility in Fe [64,65] is observed compared to Mn in Fe [12]. It is worth to notice that the total binding energy of CuMn clusters is higher than that of NiMn clusters; an effect that is also reproduced by the potential.

Finally, we mention that the $\langle 110\rangle$ CuMn is unstable both according to DFT and potential.

In Fig. 3 the Mn solubility limit in Cu obtained from Calphad calculations [66,67] and the potential are compared. We notice that the uncertainty on the Calphad calculations is large and the chosen parameterizations represent the limiting cases. The solubility limit predicted by the potential lays between the limiting cases.

5. Thermal stability of nickel-manganese-copper clusters

In this section we present the results from exchange Monte Carlo in isobaric grand canonical ensemble using the above developed potential. We thus provide an estimate of the solubility of NiMn and NiMnCu clusters in a bcc Fe matrix.

In Fig. 4 the NiMn solubility limit for the FeNiMn alloy is presented. Clearly there exists a synergy between Ni and Mn, as the addition of either element elevates the solvus by up to 150 K compared to the binary FeNi and FeMn solubility limits; or, alternatively, at any given temperature in the range considered the solubility limit moves towards smaller concentrations. The latter is consistent with the thermodynamic calculations in [6].

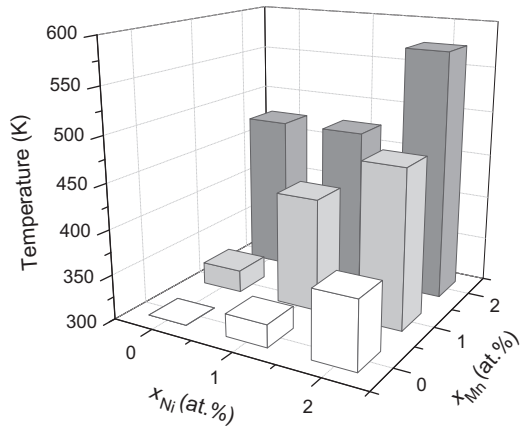

Fig. 4. The NiMn solubility limit in the ternary FeNiMn alloy resulting from the MMC simulations.

For the ternary alloys exhibiting phase separation with concentrations $x_{Ni} \geqslant x_{Mn}$ we found the coexistence of two phases in the form of the Fe-rich matrix and a single NiMn precipitate. The latter precipitates are nearly spherical and composed of an equimolar Ni and Mn fraction with a negligible amount of Fe. In fact, closer inspection reveals that the B2 intermetallic is formed, as shown in Fig. 5a. The formation of this intermetallic can be rationalized from the NiMn phase diagrams where an intermetallic at 50%Mn (Ni) occurs. The excess amounts of Ni are soluble in the Fe-rich matrix.

For the ternary alloys exhibiting phase separation with concentrations $x_{Ni} < x_{Mn}$ we found the coexistence of three phases in the form of the Fe-rich matrix, a single B2 ordered NiMn precipitate and an additional Mn-rich precipitate. Both precipitates are nearly spherical (containing a negligible amount of Fe) and the latter contains ~20% of Ni homogeneously distributed in the Mn-rich precipitate, as visualized in Fig. 5b.

The addition of 0.5% Cu (well beyond the Cu solubility in Fe) to the ternary FeNiMn alloy has a significant impact on the phase diagram. Two situations are identified: (i) the Cu precipitates together with Ni and Mn forming a ternary phase (see Fig. 6a) and (ii) the Cu precipitates without active involvement of Ni and Mn (see Fig. 6b). In the first situation, a nearly spherical precipitate is formed consisting of a mixture of ~20% Cu, ~40% Ni and ~40% Mn, as visualized in Fig. 6a. The second situation involves a nearly spherical Cu precipitate with a dilute shell of Ni and Mn atoms attached to it, similar to the observation of Cu-rich precipitates with a dilute Ni shell in supersaturated FeNiCu alloys [25].

It is interesting to note that similar type of NiMn and CuNiMn clusters were found in the work of Odette and Wirth [4]. In particular, for quaternary alloys containing 0.4% Cu, 1.4% Mn and various amounts of Ni ($x_{Ni} < x_{Mn}$) in the temperature range 533–566 K they observed nearly pure Cu clusters surrounded by a patchy Mn and Ni shell. For the highest Ni contents (>1.12% Ni), the NiMn shell was ordered or grown as an appendage epitaxial to a nearly pure Cu region. Judging from our results, the latter observation probably indicates a three phase region: (i) Fe-rich matrix, (ii) NiMn ordered phase (see Fig. 5a) and (iii) Cu precipitate with NiMn shell (see Fig. 6b). As shown below (see Fig. 7), the selected temperature and composition ranges probably prohibit the formation of the ternary CuNiMn phase. We conclude that the present results are not in contradiction with the findings in [4].

In Fig. 7 we compare the solubility limit for the FeNiMn (for equal Ni and Mn content) with the one containing an additional 0.5% Cu. For clarity, we identified situation (i) as phase separation while situation (ii) was identified as full solubility of Ni and Mn.

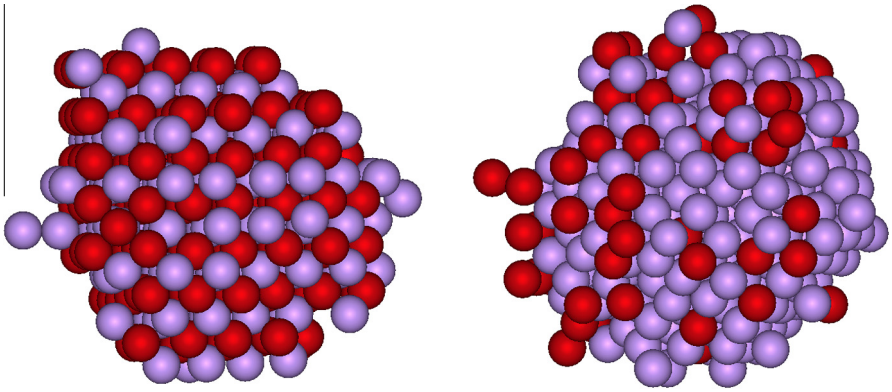

Fig. 5. Precipitate (a) B2 and (b) Mn-rich precipitates. The red (dark) atoms denote Ni while the purple (light) atoms denote Mn. (For interpretation of the references to colour in this figure legend, the reader is referred to the web version of this article.)

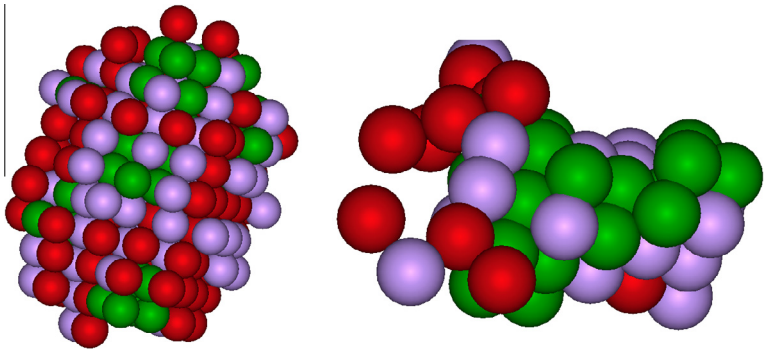

Fig. 6. Precipitate (a) ternary CuMnNi rich precipitate. The red (dark) atoms denote Ni, the purple (light) atoms denote Mn and the green (grey) atoms denote Cu. (For interpretation of the references to colour in this figure legend, the reader is referred to the web version of this article.)

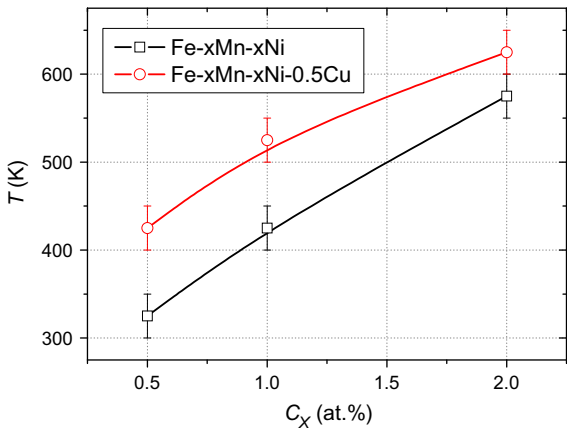

Fig. 7. Comparison of MnNi solubility with or without addition of 0.5% Cu.

We observe a clear synergistic effect of Cu on the solubility limit, raising the latter by 50 K up to 100 K. This means that ternary CuNiMn precipitates may become thermodynamically stable at reactor temperature (~600 K) with sufficiently high Cu and Ni levels.

6. Discussion

We fitted a quaternary interatomic potential to DFT and experimental data of relevance for the study of irradiation effects in the FeNiMnCu alloy. DFT calculations predict instability of NiMn pairs and triplets. However, additional DFT calculations show that NiMn clusters are stable above a certain size. This suggests that it is possible to stabilize NiMn clusters in Fe.

We used the developed potential to study the thermal stability of NiMn(Cu) clusters and verified that the synergy of both or all three elements may indeed lead to stable precipitation at reactor temperature (~600 K), especially if Cu is present in relatively high concentration. Compared to the solubility limit of the binaries, in general we can say that the synergy between Ni and Mn raises the solubility limit by ~100–150 K, while an additional 0.5% Cu raises it by another ~50–100 K. Thus the synergy of Ni, Mn and Cu can raise the solubility limit by up to ~200 K, correspondingly pushing the solvus towards progressively lower concentrations at a given temperature. From the results of Fig. 7, we observe that, in Fe–2%Mn–%2Ni, precipitates would form up to 575 K and the addition of 0.5% Cu would raise this temperature further up to 625 K. This is about 60–70 K higher than the typical reactor's operating temperatures, although of course such a large amount of these solutes is never found in RPV steels. From Fig. 4 we can say that, for a realistic composition of about 1%Ni and 1%Mn, the solvus will be at 450–500 K, so ~50–100 K below the reactor's operating temperature, but the addition of enough Cu might raise the solvus enough to make precipitation thermodynamically possible, although probably the amount of Cu required would exceed the typical Cu content of RPV steels.

As a matter of fact the above analysis is conservative, due to a shortcoming in the FeNi part of the potential. While both FeMn and FeCu were especially fitted to the experimental solubility limit, the FeNi potential was not. Emphasis was put on reproducing the experimentally observed intermetallic phases [32]. As a consequence, the FeNi potential overestimates the experimental Ni solubility in bcc Fe [14] by about a factor five, as shown in Fig. 8. In

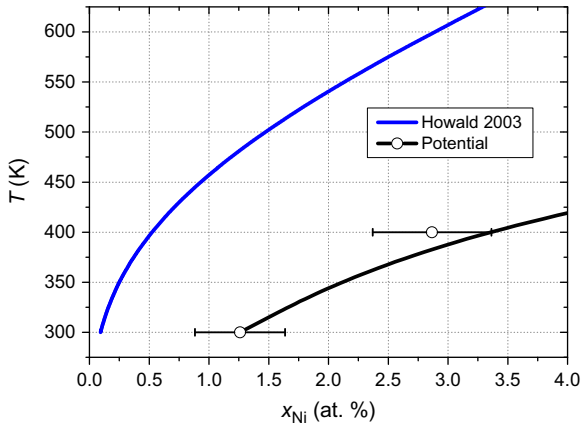

Fig. 8. Comparison between FeNi phase diagrams resulting from thermodynamic models and the potential.

turn, this means that, although all presented results are qualitatively meaningful, the lowest temperature here reported at which precipitates are observed is only a lower boundary. Given the overestimation of the Ni solubility in the binary alloy, the synergy of Ni and Mn might raise the solvus by up to 300 K, resulting in precipitation up to ~725 K and higher for high Ni and Mn content (~2%), when accounting also for the effect of 0.5% Cu. This is more than 150 K above the reactor's operating temperature. It is therefore not impossible that, at the reactor's operating temperature, NiMn and especially NiMnCu precipitates are thermodynamically stable phases.

Nonetheless, the present study does not elucidate whether the operating conditions (temperature and fluence) would allow the thermodynamic equilibrium state to be actually reached. When considering the reactor's operating temperature, for typical solute contents, one sees that it is very close to the solubility limit, i.e., the system under reactor conditions will generally be only barely inside the miscibility gap. Thus, the thermodynamic driving force (i.e. chemical potential) for the formation of MNP will be limited compared to e.g. the one for CRP in high Cu RPV steels and very little variations in composition or temperature might determine whether or not the system is actually inside or outside the miscibility gap. Much will depend on the efficiency of the kinetics leading to precipitation. This might explain why the actual observation of "late-blooming" effects, and especially their effect on mechanical properties, are often elusive and requires relatively low irradiation temperature [69]. At the same time, the fact that even in the best case the composition would be very close to the solvus suggests that it is very unlikely that large volume fractions of MNPs can ppear all of a sudden.

Let us consider now the energy barriers for the different mechanisms that can realize mass transfer. Under thermal annealing condition these are vacancies. The vacancy solute migration barriers are [58], 0.56 eV for Cu, 0.65 eV for Fe, 0.70 eV for Ni and 1.03 eV for Mn. Therefore Cu atoms will re-distribute faster than the Ni ones and Mn will be almost immobile at reactor operating temperature, compared to Cu, Ni and Fe. In other words, under thermal ageing conditions it might prove impossible or very difficult to form MnNi clusters, especially without, or in presence of very little, Cu, even if they were thermodynamically stable.

When considering irradiation, however, the vacancy fluxes drastically increase. Moreover, another mechanism for mass transfer is activated, i.e., self-interstitial diffusion. As only Mn and Fe form stable interstitials, they are the only elements that can be transported in this way. Given their migration barriers of 0.34 eV [68], they diffuse equally fast as self-interstitials in Fe and considerably faster than vacancy mediated diffusion, although their steady-state concentration is likely to be considerably lower than the vacancy concentration, depending on the sink population. Thus, while the rearrangement of Cu and Ni is expected to be mainly driven by vacancy diffusion, the rearrangement of Mn (and Fe) is expected to be mainly driven by self-interstitial diffusion. The higher efficiency of Mn transport over Ni and Cu transport is likely to explain why Mn is observed to precipitate first [6,7,10]. Moreover, transport via self-interstitials would be the origin of the presence of these point-defects in MNPs, and might also be catalysing precipitation, consistently with the prediction of the model proposed in [10]. Yet another effect that would only appear under irradiation and possibly lead to faster nucleation of precipitates than under thermal ageing, even irrespective of their thermodynamic stability, is the segregation at point-defect clusters of solutes transported by point-defects.

The question of whether the above mechanisms form an additional driving force towards the formation of stable NiMn and NiMnCu precipitates, however, together with the actual role of nucleation on point-defect clusters as a mechanism to catalyse precipitation, is at present the subject of speculation. Yet these details are important, because the thermodynamic stability of the precipitates or their association with point-defects might influence significantly the strength of their interaction with dislocations. To clarify this question the development of nanostructure and microchemical evolution models that treat simultaneously point-defect cluster formation and solute transport is necessary. The present potential can contribute to the parameterization of such models. It can equally be used in molecular dynamics simulations to estimate the dislocation obstacle strength of the outcome of the process of precipitation, whichever the mechanism. These are the objectives of future work.

7. Conclusion

We developed an interatomic potential for the FeCuNiMn quaternary alloy based on extensive DFT data on solute–solute and solute-point defect interaction, as well as on experimental data, always privileging experimental consistency within the unavoidable series of compromises that have to be made in the fitting process.

The reference DFT data on solute–solute interaction reveal that, while Mn–Ni pairs and triplets are unstable, larger clusters are actually kept together by attractive binding energy. Thus, the formation of thermodynamically stable Mn–Ni-rich phases in Fe is actually possible and this fact is accounted for by the potential, in agreement with Calphad predictions, thereby removing the apparent discrepancy of the latter with DFT, if only pairs and triplets are considered.

The Ni–Mn synergy increases significantly the temperature range of stability of solute atom precipitates in Fe as compared to binary alloys. Cu is found to extend the range of thermodynamic stability of the precipitates even further, thereby explaining the observations of MNPs, and making their appearance possible in RPV steels, even under thermal ageing and in the absence of Si. Nevertheless, under reactor conditions (temperature, composition...), the system will be barely inside the miscibility gap: small variations in temperature and composition will determine significantly different thermodynamic conditions in terms of precipitate stability, making the production of sufficient volume fractions of these phases to observe a late blooming effect rather elusive. It is therefore speculated that the appearance of Mn–Ni-rich precipitates under irradiation, irrespective of their thermodynamic stability, is actually made kinetically possible by the massive fluxes of point-defects and by point-defect cluster formation, that are strictly the consequence of irradiation.

The mechanism leading to the formation of the so-called late blooming phases, or more correctly Mn–Ni-rich clusters (with

inclusion or not of point-defects), as well as their actual thermodynamic stability under reactor conditions, are assumed to influence their strength as obstacles to dislocation motion, thereby determining (or not) a visible change in the mechanical response of the material after their appearance. The interatomic potential presently developed is expected to contribute significantly to unravel these still open issues.

Acknowledgements

This work was performed in the framework of the EC-funded FP7/PERFORM60 project, under grant agreement 232612. A part of this work was carried out using the HELIOS supercomputer system at Computational Simulation Centre of International Fusion Energy Research Centre (IFERC-CSC), Aomori, Japan, under the Broader Approach collaboration between Euratom and Japan, implemented by Fusion for Energy and JAEA. GB is grateful to N. Baetens for useful discussions.

Appendix A:. potential parameterization

Given the ternary FeNiCu potential [25], the pair potentials V are parameterized as,

Table A1
The optimized parameter set for the present potential.

MnMn			
k	r_k (Å)	a_k (eV Å^{-3})	
1	2.00000000E + 00	1.00000000E + 02	A = −1.82507983E + 00 eV
2	2.50000000E + 00	4.08563703E + 00	B = 9.12539918E-01 eV
3	2.68750000E + 00	−9.53987268E-02	C_0 = 2.29590248E-02
4	2.87500000E + 00	−3.61659426E + 00	r_0 = 4.00000000E + 00 Å
5	3.06250000E + 00	5.80612286E + 00	
6	3.25000000E + 00	−3.92221726E + 00	
7	3.43750000E + 00	3.15773891E + 00	
8	3.62500000E + 00	−5.40379206E + 00	
9	3.81250000E + 00	5.73167705E + 00	
10	4.00000000E + 00	−2.17285477E + 00	
FeMn			
k	r_k (Å)	a_k (eV Å^{-3})	
1	2.00000000E + 00	1.94252170E + 02	
2	2.32857143E + 00	−9.30366408E + 00	
3	2.40000000E + 00	2.50000000E-01	
4	2.65714286E + 00	3.91455751E + 00	
5	2.98571429E + 00	−4.60199252E + 00	
6	3.31428571E + 00	6.24436003E + 00	
7	3.64285714E + 00	−3.79624807E + 00	
8	3.97142857E + 00	1.20087815E + 00	
9	4.30000000E + 00	−2.17700581E-01	
NiMn			
k	r_k (Å)	a_k (eV Å^{-3})	
1	2.00000000E + 00	6.25441631E + 01	
2	2.23142857E + 00	5.09238791E + 00	
3	2.30000000E + 00	2.50000000E + 00	
4	2.46285714E + 00	2.56431281E + 00	
5	2.69428571E + 00	−9.63005933E + 00	
6	2.92571429E + 00	2.02436170E + 01	
7	3.15714286E + 00	−2.20193779E + 01	
8	3.38857143E + 00	1.38210959E + 01	
9	3.62000000E + 00	−3.71026389E + 00	
CuMn			
k	r_k (Å)	a_k (eV Å^{-3})	
1	2.00000000E + 00	6.24913195E + 01	
2	2.30000000E + 00	3.55000000E + 01	
3	2.31428571E + 00	3.44649496E + 00	
4	2.62857143E + 00	−2.91539938E-01	
5	2.94285714E + 00	1.58453589E + 00	
6	3.25714286E + 00	−8.34895346E-01	
7	3.57142857E + 00	−1.07164946E-01	
8	3.88571429E + 00	7.17045029E-01	
9	4.20000000E + 00	−3.62350526E-01	

$$V(r) = \sum_{k=1}^{N_p} [a_k (r_k - r)^3 \Theta(r_k - r)] \tag{A1}$$

with a_k the spline coefficients, r_k the knots and Θ is the Heaviside function. The density function φ is parameterized as,

$$\varphi(r) = C_0 (r_0 - r)^3 \Theta(r_0 - r), \tag{A2}$$

with r_0 the cut-off knot and C_0 a normalization factor. The embedding function F is parameterized as,

$$F = A\sqrt{\rho} + B\rho \tag{A3}$$

with A and B fitting parameters. The optimized parameter set for the present potential is summarized in Table A1.

References

[1] C.A. English, W.J. Phythian, R.J. McElroy, Mater. Res. Soc. Symp. Proc. 439 (1997) 471.
[2] G.R. Odette, G.E. Lucas, Rad. Eff. Def. Sol. 144 (1998) 189.
[3] G.R. Odette, R.K. Nanstad, JOM 61 (2009) 17.
[4] G.R. Odette, B.D. Wirth, J. Nucl. Mater. 251 (1997) 157.
[5] P. Pareige, J.C. Van Duysen, P. Auger, App. Surf. Sci. 67 (1993) 342.
[6] E. Meslin, B. Radiguet, P. Pareige, A. Barbu, J. Nucl. Mater. 399 (2010) 137.
[7] E. Meslin, B. Radiguet, P. Pareige, C. Toffolon, A. Barbu, Exp. Mech. 51 (2011) 1453.
[8] G.R. Odette, Mater. Res. Soc. Symp. Proc. 373 (1995) 137.
[9] C.L. Liu, G.R. Odette, B.D. Wirth, G.E. Lucas, Mater. Sci. Eng. A 238 (1997) 215.
[10] R. Ngayam-Happy, C.S. Becquart, C. Domain, L. Malerba, J. Nucl. Mater. 426 (2012) 198.
[11] M. Hansen, K. Anderko, Constitution of Binary Alloys, McGraw-Hill Book Co., 1958.
[12] W. Huang, Calphad 13 (1989) 243.
[13] R.A. Howald, Metall. Mater. Trans. A 34 (2003) 1759.
[14] T.B. Massalski, H. Okamoto, Binary Alloys Phase Diagrams, 2nd ed., Plenum, New York, 1996.
[15] J.O. Andersson, T. Helander, L. Höglund, P.F. Shi, B. Sundman, Calphad 26 (2002) 273.
[16] A.T. Dinsdale, Calphad 15 (1989) 317.
[17] E. Vincent, C.S. Becquart, C. Domain, J. Nucl. Mater. 382 (2008) 154.
[18] G. Kresse, J. Hafner, Phys. Rev. B 47 (1993) RC558.
[19] G. Kresse, J. Furthmuller, Phys. Rev. B 54 (1996) 11169.
[20] P.E. Blöchl, Phys. Rev. B 50 (1994) 17953.
[21] G. Kresse, D. Joubert, Phys. Rev. B 59 (1999) 1758.
[22] J.P. Perdew, J.A. Chevary, S.H. Vosko, K.A. Jackson, M.R. Pederson, D.J. Singh, C. Fiolhais, Phys. Rev. B 46 (1992) 6671.
[23] S.H. Vosko, L. Wilk, M. Nusair, Can. J. Phys. 58 (1980) 1200.
[24] M.S. Daw, M.I. Baskes, Phys. Rev. B 29 (1984) 6443.
[25] G. Bonny, R.C. Pasianot, N. Castin, L. Malerba, Philos. Mag. 89 (2009) 3531.
[26] M.I. Mendelev, S. Han, D.J. Srolovitz, G.J. Ackland, D.Y. Sun, M. Asta, Philos. Mag. 83 (2003) 3977.
[27] Y. Mishin, M.J. Mehl, D.A. Papaconstantopoulos, A.F. Voter, J.D. Kress, Phys. Rev. B 63 (2001) 224106.
[28] A.F. Voter, S.P. Chen, Mater. Res. Soc. Symp. Proc. 82 (1987) 175.
[29] L. Malerba, M.C. Marinica, N. Anento, C. Björkas, H. Nguyen, C. Domain, et al., J. Nucl. Mater. 406 (2010) 19.
[30] C. Domain, G. Monnet, Phys. Rev. Lett. 95 (2005) 215506.
[31] R.C. Pasianot, L. Malerba, J. Nucl. Mater. 360 (2007) 118.
[32] G. Bonny, R.C. Pasianot, L. Malerba, Modelling Simul. Mater. Sci. Eng. 17 (2009) 025010.
[33] P. Torelli, F. Sirotti, P. Ballone, Phys. Rev. B 68 (2003) 205413.
[34] Y.-M. Kim, Y.-H. Shin, B.-J. Lee, Acta Mater. 57 (2009) 474.
[35] G. Bonny, R.C. Pasianot, L. Malerba, Philos. Mag. 89 (2009) 3451.
[36] M.P. Allen, D. Tildesley, Computer Simulation of Liquids, Clarendon Press, Oxford, 1987.
[37] G. Bonny, R.C. Pasianot, E.E. Zhurkin, M. Hou, Comp. Mater. Sci. 50 (2011) 2216.
[38] R. Tarumi, Y. Kawasaki, Y. Tabe, H. Ogi, M. Hirao, T. Kagayama, Jap. J. Appl. Phys. 45 (2006) 4487.
[39] P.W. Bridgman, E.A. Mason, Collected experimental papers of P.W. Bridgman 33 (1965) 516.
[40] M. Rosen, Phys. Rev. 166 (1968) 561.
[41] K. Takemura, O. Shimomura, K. Hase, T. Kikegawa, J. Phys. F Met. Phys. 18 (1988) 197.
[42] N. Mori, M. Takahashi, G. Oomi, J. Magn. Magn. Mater. 31 (1983) 135.
[43] H. Fujihisa, K. Takemura, Phys. Rev. B 52 (1995) 13257.
[44] N. Miao, B. Sa, J. Zhou, Z. Sun, Comp. Mater. Sci. 50 (2011) 1559.
[45] R. Pasianot, D. Farkas, E.J. Savino, Phys. Rev. B 43 (1991) 6952.
[46] O. Yifang, Z. Bangwei, L. Shuzhi, J. Zhanpeng, Z. Phys. B 101 (1996) 161.
[47] Z. Bangwei, O. Yifang, L. Shuzhi, J. Zhanpeng, Phys. Rev. B 262 (1999) 218.
[48] P. Marshall, Austenitic Stainless Steels: Microstructure and Mechanical Properties, Elsevier Applied Sciences, 1984.
[49] D. Hobbs, J. Hafner, D. Spisak, Phys. Rev. B 68 (2003) 014407.

[50] J. Hafner, D. Hobbs, Phys. Rev. B 68 (2003) 014408.
[51] C. Kittel, Introduction to Solid State Physics, John Wiley & Sons, New York, 1996.
[52] H. Okamoto, Phase Diagrams of Binary Iron Alloys, ASM International, Materials Park, OH, 1993.
[53] T. Jo, K. Hirai, J. Phys. Soc. Jpn. 55 (1986) 2017.
[54] H. Uchishiba, J. Phys. Soc. Jpn. 31 (1971) 436.
[55] M. de Koning, A. Antonelli, Phys. Rev. E 53 (1996) 465.
[56] M. de Koning, A. Antonelli, S. Yip, J. Chem. Phys. 115 (2001) 11025.
[57] R.A. Johnson, Phys. Rev. 134 (1964) A1329.
[58] E. Vincent, C.S. Becquart, C. Domain, J. Nucl. Mater. 351 (2006) 88.
[59] P. Olsson, T.P.C. Klaver, C. Domain, Phys. Rev. B 81 (2010) 054102.
[60] E. Vincent, C.S. Becquart, C. Domain, Nucl. Instr. Meth. Phys. Res. B 255 (2007) 78.
[61] B.R. Coles, W. Hume-Rothery, J. Inst. Met. 80 (1951) 85.
[62] A. Lasserre, F. Reynaud, P. Coulomb, Scr. Metall. 12 (1978) 715.
[63] N.A. Gokcen, J. Phase Equil. 12 (1991) 313.
[64] G. Salje, M. Feller-Kniepmeier, J. Appl. Phys. 48 (1977) 1833.
[65] M. Perez, F. Perrard, V. Massardier, X. Kleber, A. Deschamps, H. de Monestrol, P. Pareige, G. Covarel, Philos. Mag. 85 (2005) 2197.
[66] K. Lewin, D. Sichen, S. Seetlaraman, Scand. J. Metall. 22 (1993) 310.
[67] J. Vrestal, J. Stepankova, P. Broz, Scand. J. Metall. 25 (1996) 224. Data were modified by A.T. Dinsdale (7/3/2000) to avoid bcc phase being stable in regions where it should not be stable.
[68] E. Vincent, C.S. Becquart, C. Domain, J. Nucl. Mater. 359 (2006) 227.
[69] F. Bergner, A. Ulbricht, H.W. Viehrig, Philos. Mag. Lett. 89 (2009) 795.